

2
3 **Towards the maximum efficiency design of a perovskite solar cell by**
4 **material properties tuning: A multidimensional approach**

5
6 Manfred G. Kratzenberg^{1,2*}, Ricardo Rütger² & Carlos R. Rambo¹

7
8 ¹ *Electrical Materials Laboratory (LAMATE), Department of Electrical Engineering, Universidade Federal de Santa Catarina (UFSC), Florianópolis*
9 *88040-970, SC Brazil*

10 ² *Fotovoltaica UFSC – Solar Energy Research Laboratory, Universidade Federal de Santa Catarina (UFSC), Florianópolis 88056-000, SC Brazil.*

11 **ABSTRACT**

12
13 In order to obtain significant increases in the Power Conversion Efficiency (PCE) of solar cells, we
14 argue that future cell research and development should be based on the concomitant improvement of
15 multiple material properties, rather than on the state-of-the-art one- or two-dimensional
16 improvements. In this context, researchers should know, which combined material properties and cell
17 design parameters lead to the highest efficiency increase. For the same objective, it should also be
18 known which relationships in-between these variables have to be adjusted. Such knowledge becomes
19 available by simulation and numerical optimization, which we present for a Perovskite Solar Cell
20 (PSC) in a hypercube space of variables. We prove that its PCE increases principally because of the
21 nonlinearities of this model in the multidimensional space, elucidating the importance of the
22 concomitant variable improvement in the PSC optimization. In the most optimal case, efficiencies of
23 at least 27.6% can be obtained by the simultaneous improvement of the cell's material properties,
24 and light trapping, for a large range of absorber layer thickness of $t_0 = 160...400$ nm. The lower
25 thickness value results in a significant reduction of the cell's lead (Pb) content.

26
27 **Keywords:** Perovskite solar cells, Simulation, Numerical optimization, Light trapping, Cell designs.

28
29 * Corresponding author.

30 E-mail address: manfredkratzenberg@gmail.com (M. Kratzenberg)

31
32 **1. Introduction**

33 Early research in hybrid solar cells (Huang and Huang, 2014; O'Regan and Grätzel, 1991; Wong et
34 al., 2007) led to the concept of the so-known PSC (Kojima et al., 2009), a hybrid thin-film cell,
35 which absorber layer is constituted by an organic-inorganic compound of semiconductor materials.

36 In searching for new materials and properties of this cell, more recent advances provided the steepest
37 PCE increase in comparison to all other types of cells, reaching the state-of-the-art efficiency of

1 24.2% for a manufactured prototype (NREL, 2019). Several attempts were accomplished in order to
2 reduce the toxicity inherent to the heavy-metal Pb, present in the absorber layers of high-efficiency
3 PSCs. Such methods consider the complete (Devi and Mehra, 2019; Dixit et al., 2019), or partial
4 substitution of this element (Liu et al., 2018). However, they lead in much lower PCE, if compared to
5 the state-of-the-art efficiency. Our objective is to provide more knowledge and insights about the
6 optimization process of perovskite solar cells and propose high-efficiency designs for future PSC
7 developments. To access this knowledge, and the design concepts, we propose a multidimensional
8 numerical optimization of a cell's drift-diffusion model. Our design concepts show, that the state-of-
9 the-art PCE can be significantly increased, while the Pb content can be reduced up to an order of
10 magnitude.

11

12 **2. Optimization of perovskite solar cells**

13 State-of-the-art PSCs are mostly optimized based on cell prototyping, where the cell's efficiency is
14 increased in small steps as a function of one or two different variables, as permitted by graphical
15 visualization in one- or two-dimensional function spaces. This has the inherent disadvantage that
16 variations in the not measured material properties are unknown. Therefore, an efficiency gain by
17 reason of the improvement of one, or more, of the material properties can be completely or partially
18 nullified by the worsening of other, not controlled, properties. This situation should be better
19 controlled in future cell manufacturing.

20 The benefits of mathematical modeling of the PSC's efficiency, by use of an analytical model
21 (Kratzenberg et al., 2015; Sun et al., 2015; Taretto et al., 2017), a numerical model (Amu, 2014; Azri
22 et al., 2019; Devi et al., 2018; Dixit et al., 2019; Foster et al., 2014; Iftiqar and Yi, 2016; Kanoun et
23 al., 2019; Liu et al., 2014; Ren et al., 2017; Zhao et al., 2018), or a combination of these models
24 (Agarwal and Nair, 2014, 2015), as used to interpret the cell's drift-diffusion equations, can result in
25 valuable understanding, and accelerate potentially the cell's development process. Similar analytical
26 solutions of the drift-diffusion model were earlier introduced for organic solar cells (Jiang et al.,

1 2015; Chowdhury and Alam, 2014). Finite-difference modeling schemes, which present a better
2 accuracy, because of its higher resolution, are likewise, used to solve these equations (Zandi and
3 Razaghi, 2019), or to simulate the cell's short circuit current density (J_{sc}) increase by reason of light
4 trapping (Cai et al., 2015). Some authors also present an efficiency optimization in a one-
5 dimensional optimization of the cells charge conduction layer thickness (Kim and Ohkita, 2017;
6 Zhao et al., 2018). Simulation studies based on the drift-diffusion models lead already in high
7 efficiency values of 25% for single-junction PSCs (Agarwal and Nair, 2014, 2015). The drift-
8 diffusion models simulate the cell's current-voltage curve typically as a function of multiple material
9 properties and the absorber layer thickness. Considering arbitrary material property improvements at
10 different improvement scales, the efficiency of this model can be increased by a multidimensional
11 optimization algorithm. Multidimensional optimizations are state-of-the-art to solve many
12 engineering problems in order to find, e.g. (i) the optimal power flow in electric power grids (Crow,
13 2009), (ii) the lowest cost design of a wind turbine synchronous generator (Bazzo et al., 2017), or the
14 minimal series resistance in a GaAs solar cell (Algora and Díaz, 2000).

15 In the analyses of a cell's drift-diffusion model, a multidimensional optimization is useful in order to
16 demonstrate that the concomitant variable improvement results in much higher efficiency increases
17 than in state-of-the-art one- and two-dimensional optimization techniques. Additionally, the
18 multidimensional optimization can lead (i) to a better understanding of the optimization process and
19 (ii) to the proposal of advanced solutions for future high-efficient solar cell design concepts as here
20 proposed.

21 While the highest state-of-the-art PCE of a manufactured PSC is already 24.2% (NREL, 2019),
22 perovskite solar cells show still a high improvement potential. Considering in a simplified PSC
23 model, only optical recombination losses, the maximal efficiencies of 30% (Yin et al., 2014), 30.88%
24 (Sha et al., 2015) and 31.3% (Martynov et al., 2017) can theoretically be obtained in single-junction
25 PSCs. Furthermore, using zero surface recombination velocities and ideal light trapping in a drift-
26 diffusion model, a PCE of 29.9% can be obtained (Ren et al., 2017). These upper limits are below the

1 highest attainable PCE of single-junction cells, which thermodynamic limit is calculated with 33.7%
2 for the black-body (Shockley and Queisser, 1961), and 33% for the measured irradiation spectrums
3 (Rühle, 2016).

4 However, in manufactured solar cells, additional recombination losses appear because of a cell's
5 non-ideal material properties. Based on the results from our multidimensional optimizations, we
6 propose cell designs that increase the efficiency of the state-of-the-art manufactured and simulated
7 PSCs. The same proposed cell designs present also a much lower Pb content. The high efficiency of
8 these cell designs is based on high-resolution J_{sc} simulations of efficient light trapping schemes, and
9 we show how the PCE can be increased further, by additional tuning of the cell's material properties.
10 Similar design concepts can be found presently only for manufactured solar cells with much lower
11 PCE, in comparison to state-of-the-art cells (Liu, 2017), or otherwise, only for simulations of the J_{sc}
12 values (Cai et al., 2015). The former author shows that the efficiency of a manufactured PSC, with a
13 100 nm thick absorber layer, can increase from 5.8% to 7.1% by light trapping; and the latter authors
14 present a finite-difference time-domain simulation (FDTD), which shows that plasmonic light
15 trapping can lead in a 2.15-fold increase of the J_{sc} value, in PSC with a 50 nm thin absorber layer, if
16 compared to a cell of this thickness without light trapping.

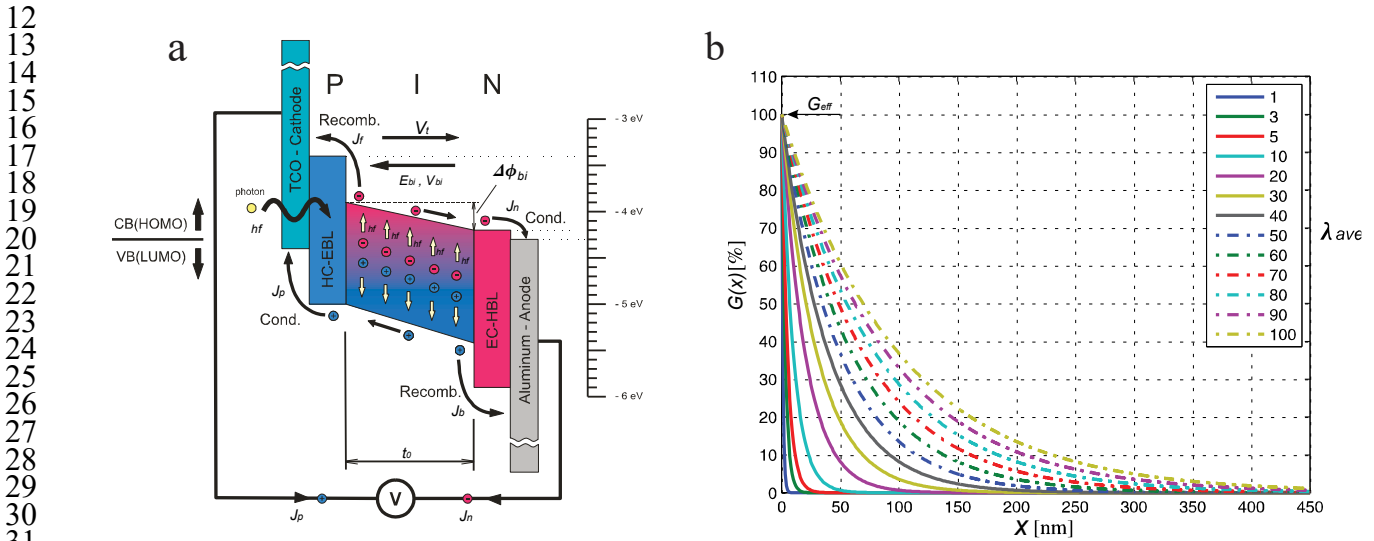
17

18 **3. Methodology - Optimization in a hypercube space of variables**

19 To develop a PSC, which shows the highest possible PCE, some fundamental questions should be
20 answered. These are: (i) which multiple material properties and cell design parameters are necessary
21 to be improved concomitantly, (ii) has the value for each of the considered variables to be increased
22 or decreased, and (iii) to which value each of these model variables should be ideally tuned. Using a
23 drift-diffusion model, these questions can be answered by searching the maximal efficiency in a
24 multidimensional function space of material properties and manufacturing parameters.

25 In the present optimizations, we select an analytical solar cell model, as introduced in (Sun et al.,
26 2015), which efficiency we maximized by a numerical optimization method and the simplifications

1 of this model are discussed in Appendix B1.1. The selected model and method reduce significantly
 2 the computational optimization cost if compared to a numerical PSC model and random search
 3 methods. This enabled us to accomplish a large set of optimizations, using different constraints in
 4 each of these optimizations, for the model's variable set. The approximations made by the selected
 5 analytical model results in a low fitting deviation of only 0.1%, between the measured and the
 6 simulated PCE values (Sun et al., 2015). This small deviation is insignificant considering that
 7 outdoor spectral variations can lead to PCE uncertainties of 3% in thin-film cells (Rüther et al.,
 8 2002). The used model was elaborated in from (i) the second-order Poisson differential equation and
 9 its two boundary equations and (ii) a further set of four second-order drift-diffusion differential
 10 equations, and its boundary equations, which describe the cell's electron and hole transports in the
 11 dark and under exposition to light (Sun et al., 2015).



33 **Fig. 1.** Energy band diagram and normalized charge generation: (a) Energy potential diagram and charge carrier trajectories of a
 34 planar pin-type heterojunction perovskite solar cell, as modeled in (Sun et al. 2015), with the following components from left to right:
 35 (i) transparent top cover (here not visualized); (ii) cathode layer made of a Transparent Conductive Oxide (TCO); (iii) p-type hole
 36 conduction and electron blocking layer, made of organic material PEDOT:PSS; (iv) i-type intrinsic charge generation layer with
 37 thickness $t_0 = 450$ nm made of the hybrid perovskite material; (v) n-type electron conduction and hole blocking layer, made of organic
 38 material PCBM; (vi) anode layer made of aluminum; adapted from supplementary information in (Sun et al. 2015). (b) Approximation
 39 of the normalized charge generation profiles $G(x)$ [$\text{cm}^{-2}\text{s}^{-1}$] per solar cell area and time as a function of the penetration depth ($x =$
 40 $0 \dots 450$ nm) on the abscissa, calculated for several of the considered average optical decay lengths of $\lambda_{ave} = 5$ to 150 nm.

42 A detailed charge transport scheme, of the used pin-type PSC, is presented in Fig. 1(a). Based on
 43 FDTD simulations (Cai et al., 2015), our optimized solar cell architectures present light trapping

1 nanoparticles in its thin absorber layers, which increase its short circuit current density (J_{sc}), if
 2 compared to the $J_{sc} = 23 \text{ mA/cm}^2$ without light trapping, in a large range of absorber layer
 3 thicknesses.

4 3.1 Modeling of the optimization

5 In this work, we propose the numerical optimization of the efficiency of PSC's analytical model in a
 6 multidimensional function space, which is specified by the following optimization problem

$$7 \quad \eta_{max} \rightarrow \max [\eta_i(X_{1,i} \dots X_{9,i})] \ ; \ i = 1 \dots N \ , \quad (1)$$

8 where the efficiency η_i in the i -th maximization iteration is a function of the nine PSC model
 9 variables ($X_{1,i} \dots X_{9,i}$), which built-up a nine-dimensional hypercube space, and where the maximum
 10 efficiency (η_{max}) is obtained after $i = 1 \dots N$ model simulations. In a single iteration of this
 11 optimization, each of the nine model variables is set up to a different value, and therefore, each
 12 iteration results in a simulation (i), where the variable values are selected by the optimization
 13 algorithm. As initial model variables ($X_1 \dots X_9$) we consider the values as obtained by the optimization
 14 in (Sun et al., 2015). In each of the N steps, the MatlabTM optimization algorithm *fmincon* improves
 15 the values of the whole set of model variables by a Nonlinear Programming (NP) optimization
 16 technique (Byrd et al., 1999), which is based on an interior point (IPM) and line search optimization
 17 methods (LSM), in order to obtain the maximal possible model efficiency. When the cell's
 18 efficiency increase is below a specified threshold value, the optimization algorithm considers that the
 19 maximal cell efficiency is obtained, and it stops the optimization process (Fig. A.2). For each of the i
 20 $= 1 \dots N$ model simulations, a new calculation of (i) the J-V curves, (ii) the maximum power point
 21 (MPP) power, and (iii) the cell's efficiency (η_i) are accomplished, using equation (2). This PCE is
 22 calculated as a function of nine model variables $X_{1,i}$ to $X_{9,i}$, which are constituted by eight quantum
 23 physical material properties and the absorber layer thickness.

$$24 \quad \eta_{MPP,i} = (U_{MPP,i} J_{MPP,i}(X_{1,i} \dots X_{9,i})) / G_{AM1.5} = P_{MPP,i} / G_{AM1.5} \quad (2)$$

1
2 In equation (2) $G_{AM1.5} = 100 \text{ mW/cm}^2$ is the normalized solar irradiation at Air Mass 1.5. The PSC's
3 maximum output power density $P_{MPP,i} [\text{mW/m}^2]$ of the i -th optimization step is obtained by the
4 maximization of its power curve in $k = 1 \dots M$ iterative steps as follows

$$P_{MPP,i} \rightarrow \max (P_k (J_{light,1} (G_{AM1.5}, V_k, X_{1,i} \dots X_{9,i}) \dots J_{light,M} (G_{AM1.5}, V_k)) ; k = 1 \dots M, \quad (3)$$

5
6
7
8 where each $P_{MPP,i}$ is related to PSC's material properties in the i -th optimization step. In order to
9 calculate $P_{MPP,i}$ the cell's analytical model uses the values of the whole set of model variables
10 ($X_{1,i} \dots X_{9,i}$) as well as the terminal voltage (V_k) and the cell's temperature as input variables to
11 calculate its current density $J_{light,k}$ under exposure to reference light ($G_{AM1.5}$). The material properties
12 are not modified in this second optimization. We remark that the power optimization of the equation
13 (3) is nested in the efficiency optimization (equation 1). This nested optimization process is subject
14 to the following specific boundary conditions

$$X_{j,min} \leq X_j \leq X_{j,max} \quad ; \quad j = 1 \dots 9, \quad (4)$$

15
16 where $X_{j,max}$ and $X_{j,min}$ are the maximal and minimal constraints for each one of the nine model
17 variables X_j to be optimized. Considering a large number of optimizations, each under different
18 boundary conditions, specific constraints of the model variables in an arbitrary optimization process
19 are given by equation (5). Each single optimization process considers a variable specific range ($X_{j,min}$
20 $\dots X_{j,max}$), in which it is allowed for the optimization algorithm to modify each of the $j = 1 \dots 9$ model
21 variables. Here we only consider for the built-in voltage (V_{bi}), the absorber layer thickness (t_0), and
22 the average optical decay length (λ_{ave}), variable specific constrains, as defined by the equations (6),
23 (7) and (9). As we cannot know which property improvements will be possible in the future cell
24 development, we set up arbitrary defined and adjustable constraints for remaining material
25 properties, by a proposed variable boundary expansion factor (f_B), as given by the following equation

$$X_{j,min} = (1/f_B) X_{j,me} \leq X_j \leq X_{j,me} (f_B) = X_{j,max} \quad ; \quad j = 1 \dots 9, \quad (5)$$

26
27

1 where the terms f_B and $1/f_B$ specify individual amplification and reduction factors in a single
 2 optimization process. The application of f_B results in the values of the upper and lower boundary
 3 limits of the model variables (X_{j-min} and X_{jmin}) in a specific efficiency optimization. In equation (5)
 4 $X_{j,me}$ represents the not expanded setup configuration of the model variables, as measured in (Sun et
 5 al., 2015), and X_{j-min} and X_{j-max} are the minima and the maxima limits as specified in equation (4).
 6 Built-in voltages with values ($V_{bi} > 1.4$ V) do not lead to any further increase of the cell's efficiency
 7 (Fig. 2(b)). Hence, the inequality constraint equation (6) is imposed additionally to the optimization
 8 in order to avoid unrealistic high values of this variable. In fact, f_B is used in this case to increase in
 9 small steps V_{bi} to the maximal value of $X_{max} = 1.4$ V (Tables 1 to 3).

$$10 \quad 11 \quad 0 \leq V_{bi} \leq 1.4 \text{ V} \quad (6)$$

12 Furthermore, we consider that each of the different available coating techniques of the absorber layer
 13 needs a specific minimal thickness (t_{0-min}) in order to avoid losses related to pinholes (Qiu et al.,
 14 2016) and conduction effects (Atwater and Polman, 2010). Therefore, we set up an additional
 15 constraint for t_0 , which considers (i) an adjustable minimum thickness (t_{0-min}) as the lower boundary
 16 in an optimization process, while (ii) the upper limit of t_0 is here assumed to be $1 \mu\text{m}$ as specified by
 17 the inequality constraint equation (7).

$$18 \quad t_{0-min} \geq t_0 \geq 1 \mu\text{m} \quad (7)$$

19 In the Beer-Lambert law λ_{ave} stands in a defined relationship with t_0 , for the consideration of low
 20 reflection losses of approximately 1% (Fig. 1b). This relation is expressed by equation (8) for the case
 21 without light trapping (Sun et al., 2015).

$$22 \quad m = t_0 / \lambda_{ave} \quad (8)$$

23 With the setup values for t_0 and λ_{ave} (section 3.2) the value of $m = 4.5$, is obtained, which should also
 24 be considered for cells with light trapping, considering similar losses. Light trapping reduces the
 25 average optical decay length (λ_{ave}) and improves at the same time the J_{sc} (Cai et al., 2015). We use the
 26 calculated $m = 4.5$ in order to specify an additional equality constraint (equation 9), here defined as the

1 m-constrained determination of λ_{ave} . In this context we calculate $\lambda_{ave}(t_0)$ for light trapping as a function
2 of t_0 , solving equation (8) for λ_{ave} as follows

$$3 \quad \lambda_{ave}(t_0) = t_0 / m = t_0 / 4.5 . \quad (9)$$

4 If λ_{ave} is instead in the same form constrained as the further model variables, by use of the f_B factor, a
5 relationship appears, as defined by the vertex lines in Figs. 2e and 2f, and Table A.3.2, which results
6 in lower λ_{ave} but higher optimized efficiency values (Tables 1 to 3 – last two columns). However,
7 improved absorption properties, and therefore, a reduced λ_{ave} , as obtained by light trapping, should
8 stand in a similar relationship to the absorber layer thickness as in a cell without light trapping, by
9 reason of the Beer-Lambert law (Fig. 1b). Therefore, we calculate an m - constrained λ_{ave} in equation
10 (9), which results in a lower PCE, and presents, therefore, a more conservative formulation. In our m
11 - constraint optimizations the remaining material properties are constrained by f_B - factor and equations
12 (6) and (7). Whereas higher efficient light trapping schemes by shape-optimized plasmonic
13 nanoparticles are possible (Kakavelakis et al., 2017), the best light-trapping scheme, as here adopted,
14 consider spherical silver (Ag) nanoparticles, which are localized at the backside of the absorber layer
15 (Cai et al., 2015). The short circuit current density for this cell configuration is, for a large thickness
16 range, higher than the value as obtained in (Sun et al., 2015). Therefore, a short circuit current density
17 correction factor for light trapping should be considered as a function of the absorber layer thicknesses,
18 which is calculated as follows

$$19 \quad CF_{lt}(t_0) = J_{sc-Cai}(t_0) / J_{sc-Sun} . \quad (10)$$

20 As without light trapping both authors presented a similar short circuit current density for the same
21 absorber material, and an absorber layer thickness of 400 nm, we can directly adopt short circuit
22 current densities as obtained by FDTD simulations in (Cai et al., 2015), in our simulation setup.

23

24

25 3.2 Setup conditions

1 We used the solar cell properties and t_0 as obtained in (Sun et al., 2015) as principal setup conditions.
2 The authors calculated by use of the OTM method, the fundamental optical parameters, which are: (i)
3 the effective generation of charge carriers, $G_{eff} = 1.4356 \times 10^{13} \text{ cm}^{-3}\text{s}^{-1}$, and (ii) the average optical
4 decay length $\lambda_{ave} = 100 \text{ nm}$, which are both specific material properties that are independent of absorber
5 layer thickness. By the derived equation for the total generation of free charge carriers (equations A.1
6 and A.2) a G_{max} of $1.4356 \times 10^{17} \text{ cm}^{-2}\text{s}^{-1}$ is calculated, which coincides with the measured short circuit
7 current density of $qG_{max} = 23 \text{ mA/cm}^2$, where q is the electric charge energy. Built-in voltage and the
8 diffusion coefficients are $V_{bi} = 0.78 \text{ V}$, and $D_n = D_p = 0.05 \text{ cm}^2/\text{s}$. The authors obtained an ideal t_0 of
9 450 nm using a one-dimensional optimization of this variable. After the manufacturing of the PSC
10 with the optimized absorber layer thickness, the authors obtained by a curve fitting: (i) the surface
11 recombination velocity of electrons in the front charge transport layer $s_f = s_n = 200 \text{ cm/s}$, (ii) the surface
12 recombination velocity of holes in the back charge transport layer $s_p = s_b = 19.2 \text{ cm/s}$, and (iii) the
13 number of the excess minority carrier concentrations of electrons and holes ($\Delta n = 8.426 \times 10^6 \text{ cm}^{-3}$, Δp
14 $= 1.3003 \times 10^8 \text{ cm}^{-3}$). Furthermore, they obtained an optimized PCE of 15.7%, in a cell with an open-
15 circuit voltage of $V_{OC} = 0.87 \text{ V}$ (Table 4 - design 6). The measured semiconductor temperature was
16 300.56 K , which results in a thermal voltage of $V_t = k_B T/q = 25.9 \text{ mV}$. As short circuit current densities
17 qG_{max} we adopted the values as obtained by the FDTD simulations in (Cai et al., 2015) for light
18 trapping with spherical nanoparticles, as a function of the absorber layer thickness of $t_0 = 50 \dots 400 \text{ nm}$
19 (equation 10).

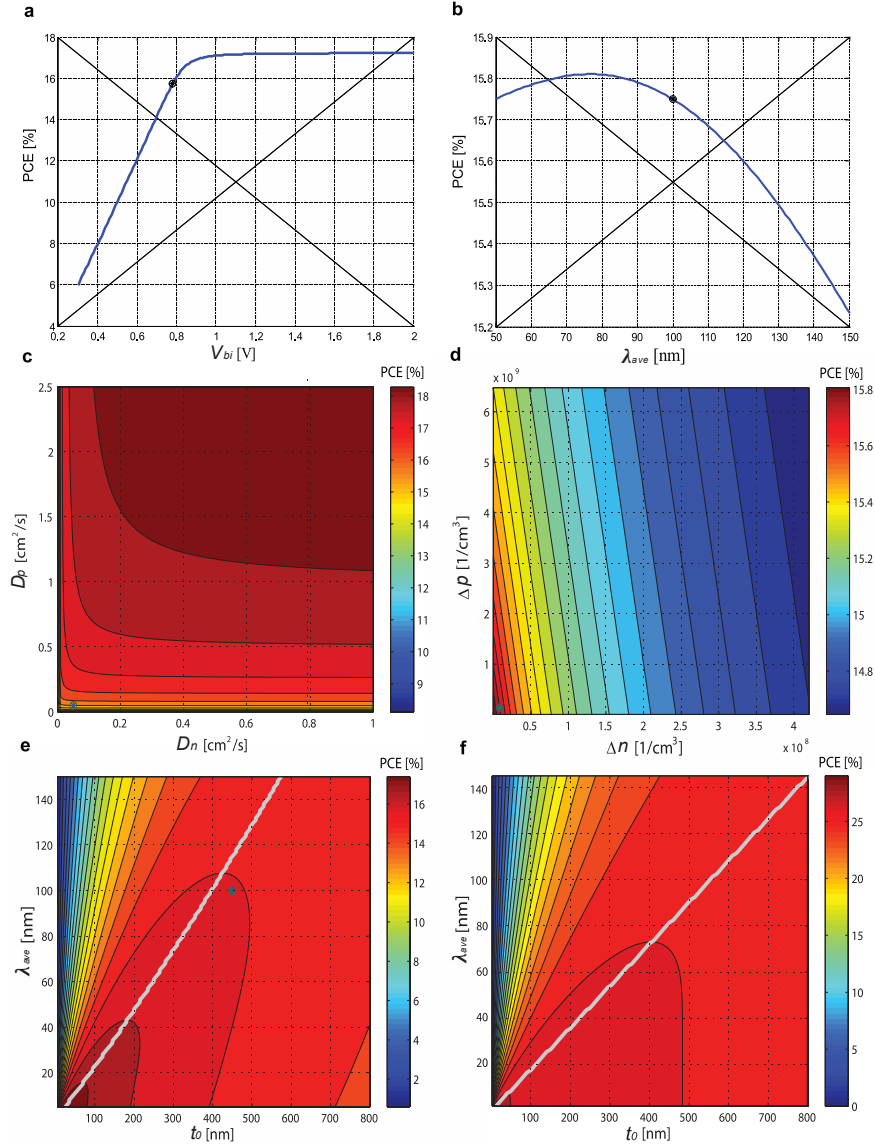
20

21 **4 Results**

22 We propose (i) a multidimensional optimization of a solar cell's efficiency, as based on its drift-
23 diffusion model, and present additionally, (ii) a complete set of the accomplishable one- and two-
24 dimensional sensitivity analyses, as obtained by the possible variable combinations. Based on our
25 results, we propose different cell designs, which increase the efficiency of state-of-the-art simulated

1 and manufactured cells. Figs. 2(a) to 2(e) show some typical one- and two-dimensional, sensitivity
2 analyses, where the efficiency is calculated as a function of the improvement of its model variables.
3

1
2
3
4
5
6
7
8
9
10
11
12
13
14
15
16
17
18
19
20
21
22



23 **Fig. 2.** One- and two-dimensional sensitivity analyses, showing the model efficiency as a function of: (a) the average optical decay
 24 length λ_{ave} ; (b) the built-in voltage V_{bi} ; (c) the diffusion coefficients of electrons and holes D_n and D_p ; (d) the excess concentration of
 25 electrons and holes Δn and Δp ; and finally, in (e) and (f), the absorber layer thickness t_0 , and the average optical decay length, where
 26 the grey vertex line shows the maximal attainable efficiency values in these two-dimensional presentations; (a) – (e) the remaining
 27 model variables are set up to the values as obtained in (Sun et al. 2015); (f) the values of the remaining model variables are set up to
 28 the values as obtained in our f_B constrained multidimensional optimization for $f_B = 160$; the measured efficiency values of 15.7% in (a)
 29 – (e) appear as a star within a surrounded circle.
 30

31 For the visualization of the efficiency gains, as obtained by the possible combinations of nine model
 32 variables, a large set of 45 such figures would be necessary. However, these figures can be
 33 substituted by Table A.1, which shows only the highest attainable PCE values of those analyses, as a
 34 function of different boundary expansion factors f_B (equation 5). For the highest variable
 35 improvement factor ($f_B = 160$) the best one- and two-dimensional efficiency optimizations increase
 36 the PCE from 15.7% to 18.1% and 20%. The Figs. 2(e) and 2(f) compare two similar two-

1 dimensional sensitivity analyses using the same model variables. While in Fig. 2(e) the remaining
2 variables confer to our setup condition, in Fig. 2(f) these variables are configured with the ideal
3 values as obtained by a multidimensional optimization with $f_B = 160$. Both figures consider light
4 trapping with independently adjustable t_0 and λ_{ave} , but the multidimensional optimization results in
5 higher efficiency values. It can be observed from the slight shift of the grey vertex lines in these
6 figures that for arbitrary values of t_0 , the multidimensional optimization demands an improved light
7 trapping, by reason of the lower optimal values of λ_{ave} for the same t_0 , if compared to the two-
8 dimensional optimization. Based on the results of our f_B - constraint multidimensional optimization,
9 as presented in Table A.2, we conclude that a variable relationship that results in maximal efficiency
10 vertex lines does only appear in-between the variables t_0 and λ_{ave} , and not in-between the further
11 model variables.

12 Fig. 3 presents six sets of 160 multidimensional optimizations ($f_B = 1 \dots 160$), for six different
13 absorber layer thicknesses. For these m -constrained optimizations the variables V_{bi} , t_0 , λ_{ave} and the
14 short circuit current densities are set up by the equations (6), (7), (9) and (10), while the remaining
15 variables are f_B - constrained. As specified in equation (7), we consider that each coating technique of
16 the absorber has its own inherent minimum thickness (t_{0-min}) for the deposition of perfect absorber
17 layers (Appendix section A.4), and therefore, we present optimized designs for different absorber
18 layer thicknesses. Light trapping with spherical nanoparticles (solid curves) presents a significant
19 efficiency advantage in comparison to the PSC without light trapping (dotted curve) in almost all
20 development states that are expressed by the f_B factor. In a 160 nm thick absorber layer, such a light-
21 trapping shows only 0.1...0.2% lower efficiencies, in comparison to the configuration with the
22 highest efficiencies ($t_0 = 400$ nm). Additionally, a PSC with $t_0 = 160$ has the advantage of presenting
23 2.5-fold lower Pb content, and therefore, we give special emphasis to this cell design in our
24 discussions.

25

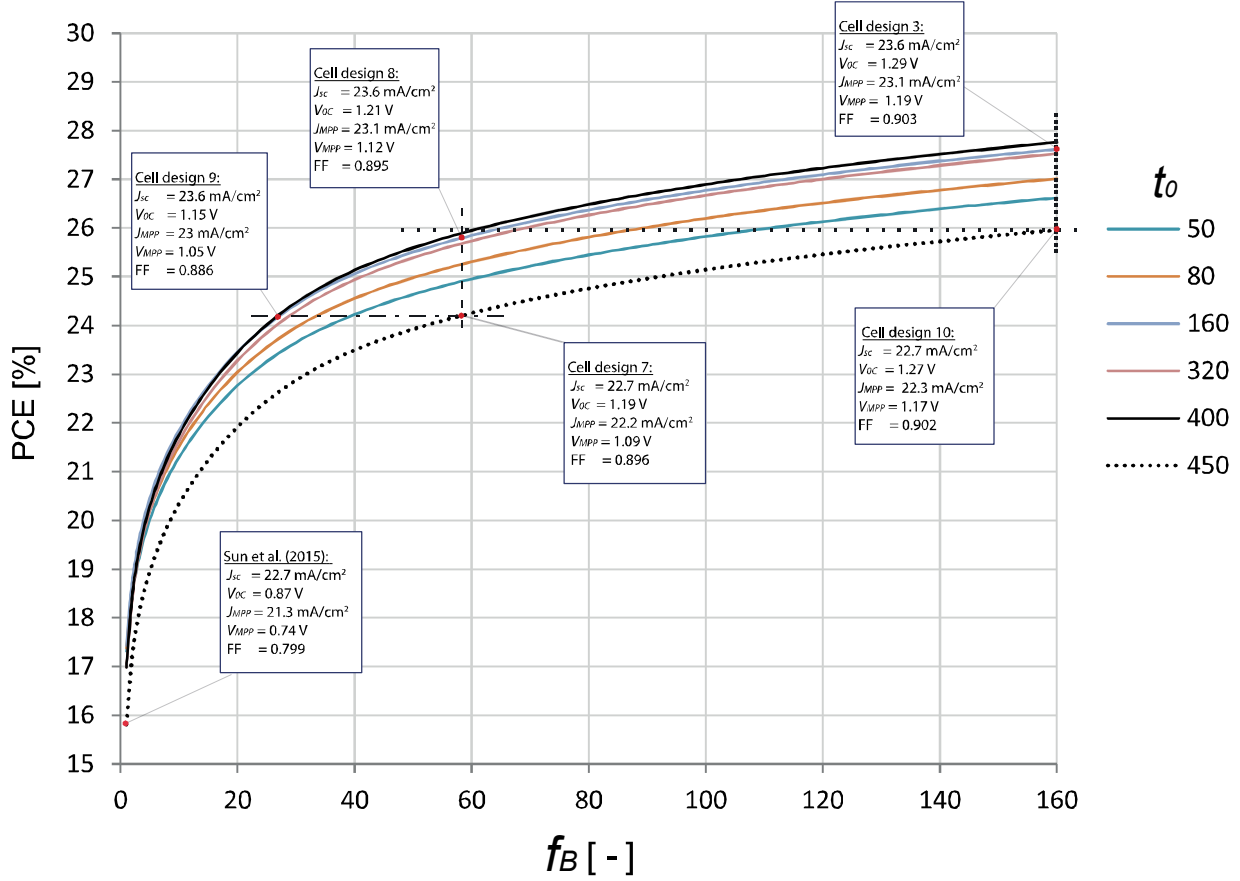


Fig. 3. Optimized efficiency as a function of the 160 boundary expansion factors ($f_B = 1 \dots 160, \in \mathbb{N}$) for six absorber layer thicknesses in the range of $t_0 = 50 \dots 450$ nm, optimization variables ($D_n, D_p, V_{bi}, s_f, s_b$), while $\lambda_{ave}(t_0) = t_0/4.5$ is the calculated average optical decay length: (i) without light trapping, $t_{0-min} = 450$ nm, $\lambda_{ave} = 100$ nm; (ii) light trapping with spherical plasmonic nanoparticles, $t_0 = 50 \dots 400$ nm, with corrected short circuit current densities. Used qG_{max} values, in unit [mA/cm^2], as obtained in (Cai et al. 2015 and Sun et al. 2015): 22.5 ($t_0 = 50$ nm), 23.05 (80 nm), 23.9 (160 nm), 24.18 (320 nm), 24.5 (400 nm), 23 (450 nm, without light trapping).

In Tables 1, 2 and 3, we show an alternative representation for some optimizations in Fig. 3, which also show the values of the optimized material properties. While Table 1 considers the state-of-the-art absorber layer thickness of 450 nm and no light trapping, Tables 2 and 3 present the results for thinner absorber layers of 400 nm and 160 nm, considering a J_{sc} as obtained by light trapping with spherical nanoparticles and a corrected λ_{ave} by equation (9). For the interested reader, we additionally show the PCE and λ_{ave} values, as obtained in optimizations with f_B -constrained λ_{ave} setups (equation 5). However, these values should be observed with caution, because of the related low reflection losses, which might be unrealistic.

Figs. 4a and 4b present, the J-V curves, and the power curves, of nine different high-efficiency design proposals. The figure visualizes in more detail, some of the simulated design proposals as

1 presented in Fig. 3. Highest efficiency designs (1) to (5) show light trapping for $t_0 = 50 \dots 400$ nm,
 2 with $f_B = 160$. While design (6) presents the cell as proposed is (Sun et al., 2015), (7) confers, as an
 3 example, to the cell with the state-of-the-art efficiency, considering improved material properties and
 4 no light trapping. Design (8) shows how (7) can be improved by light trapping, and (9) shows a
 5 similar efficiency as (7), with less ideal properties, but with light trapping. Table 4 presents the J-V
 6 performance parameters of the design proposals as shown in Figs. 3 and 4, and Table 5 visualizes the
 7 relative improvements, considering in each row the comparison of two of the design proposals, as
 8 presented in Table 4.

Table 1

Optimized model variables (boldface symbols) as obtained from optimizations in a seven-dimensional function space considering eleven optimizations with specific boundary expansion factors f_B , obtaining an ideal PSC of 25.96%, for a cell with a fixed t_0 of 450 nm, which do not use light trapping ($\lambda_{ave} = 100$ nm); $qG_{max} = 23$ mA/cm².

f_B	s_f	s_b	Δn	Δp	V_{bi}	D_n	D_p	μ_n	μ_p	t_0	λ_{ave}	η	λ_{ave}^*	η^*
[-]	[cm/s]	[cm/s]	[1/cm ³]	[1/cm ³]	[V]	[cm ² /s]	[cm ² /s]	[cm ² /Vs]	[cm ² /Vs]	[nm]	[nm]	[%]	[nm]	[%]
<i>5.00</i>	40.00	3.84	8.43E+06	1.30E+08	0.80	0.25	0.25	9.65	9.65	<i>450.00</i>	100.00	<i>18.96</i>	48.13	19.15
<i>10.00</i>	20.00	1.92	8.43E+06	1.30E+08	0.82	0.50	0.50	19.30	19.30	<i>450.00</i>	100.00	<i>20.34</i>	10.00	20.57
<i>20.00</i>	10.00	0.96	8.43E+06	1.30E+08	0.86	1.00	1.00	38.61	38.61	<i>450.00</i>	100.00	<i>21.92</i>	5.00	22.17
<i>30.00</i>	6.67	0.64	8.43E+06	1.30E+08	0.90	1.50	1.50	57.91	57.91	<i>450.00</i>	100.00	<i>22.88</i>	3.33	23.14
<i>40.00</i>	5.00	0.48	8.43E+06	1.30E+08	0.94	2.00	2.00	77.22	77.22	<i>450.00</i>	100.00	<i>23.49</i>	2.50	23.76
<i>60.00</i>	3.33	0.32	8.43E+06	1.30E+08	1.01	3.00	3.00	115.82	115.82	<i>450.00</i>	100.00	<i>24.26</i>	1.67	24.53
<i>80.00</i>	2.50	0.24	8.43E+06	1.30E+08	1.09	4.00	4.00	154.43	154.43	<i>450.00</i>	100.00	<i>24.76</i>	27.89	25.04
<i>100.00</i>	2.00	0.19	8.43E+06	1.30E+08	1.17	5.00	5.00	193.04	193.04	<i>450.00</i>	100.00	<i>25.14</i>	26.85	25.43
<i>120.00</i>	1.67	0.16	8.43E+06	1.30E+08	1.25	6.00	6.00	231.65	231.65	<i>450.00</i>	100.00	<i>25.46</i>	25.85	25.75
<i>140.00</i>	1.43	0.14	8.43E+06	1.30E+08	1.32	7.00	7.00	270.26	270.26	<i>450.00</i>	100.00	<i>25.73</i>	25.01	26.02
<i>160.00</i>	1.25	0.12	8.43E+06	1.30E+08	1.40	8.00	8.00	308.87	308.87	<i>450.00</i>	100.00	<i>25.96</i>	0.63	26.26

Observations: The values in italic formatted numbers correspond to the values of the lower curve in Fig. 3; * values obtained in f_B – constrained determination of λ_{ave}

9

10

Table 2

Optimized model variables (boldface symbols) and efficiency in seven-dimensional optimizations as a function of several boundary extension factors f_B for a PSC with $t_0 = 400$ nm, where light trapping by use of spherical nanoparticles compensates the reduced absorption in this absorber layer; $qG_{max} = 24.5$ mA/cm².

f_B	s_f	s_b	Δn	Δp	V_{bi}	D_n	D_p	μ_n	μ_p	t_0	λ_{ave}	η	λ_{ave}^*	η^*
[-]	[cm/s]	[cm/s]	[1/cm ³]	[1/cm ³]	[V]	[cm ² /s]	[cm ² /s]	[cm ² /Vs]	[cm ² /Vs]	[nm]	[nm]	[%]	[nm]	[%]
<i>5.00</i>	40.00	3.84	8.43E+06	1.30E+08	0.80	0.25	0.25	9.65	9.65	<i>400.00</i>	88.89	<i>20.29</i>	41.76	20.50
<i>10.00</i>	20.00	1.92	8.43E+06	1.30E+08	0.82	0.50	0.50	19.30	19.30	<i>400.00</i>	88.89	<i>21.76</i>	8.89	22.01
<i>20.00</i>	10.00	0.96	8.43E+06	1.30E+08	0.86	1.00	1.00	38.61	38.61	<i>400.00</i>	88.89	<i>23.45</i>	4.44	23.72
<i>30.00</i>	6.67	0.64	8.43E+06	1.30E+08	0.90	1.50	1.50	57.91	57.91	<i>400.00</i>	88.89	<i>24.47</i>	2.96	24.76
<i>40.00</i>	5.00	0.48	8.43E+06	1.30E+08	0.94	2.00	2.00	77.22	77.22	<i>400.00</i>	88.89	<i>25.13</i>	2.22	25.42
<i>60.00</i>	3.33	0.32	8.43E+06	1.30E+08	1.01	3.00	3.00	115.82	115.82	<i>400.00</i>	88.89	<i>25.95</i>	1.48	26.25
<i>80.00</i>	2.50	0.24	8.43E+06	1.30E+08	1.09	4.00	4.00	154.43	154.43	<i>400.00</i>	88.89	<i>26.48</i>	24.56	26.79
<i>100.00</i>	2.00	0.19	8.43E+06	1.30E+08	1.17	5.00	5.00	193.04	193.04	<i>400.00</i>	88.89	<i>26.90</i>	23.71	27.17
<i>120.00</i>	1.67	0.16	8.43E+06	1.30E+08	1.25	6.00	6.00	231.65	231.65	<i>400.00</i>	88.89	<i>27.23</i>	22.83	27.54
<i>140.00</i>	1.43	0.14	8.43E+06	1.30E+08	1.32	7.00	7.00	270.26	270.26	<i>400.00</i>	88.89	<i>27.52</i>	22.15	27.83
<i>160.00</i>	1.25	0.12	8.43E+06	1.30E+08	1.40	8.00	8.00	308.87	308.87	<i>400.00</i>	88.89	<i>27.76</i>	21.50	28.08

Observations: The values in italic formatted numbers correspond to the cell with $t_0 = 400$ nm in Fig. 3; * values obtained in f_B – constrained determination of λ_{ave}

11

1

Table 3

Optimized model variables (boldface symbols) and efficiencies in seven-dimensional optimizations as a function of several boundary extension factors f_B for a PSC with $t_0 = 160$ nm, where light trapping by spherical nanoparticles compensates the reduced absorption in this absorber layer; $qG_{max} = 23.9$ mA/cm².

f_B	s_f	s_b	Δn	Δp	V_{bi}	D_n	D_p	μ_n	μ_p	t_0	λ_{ave}	η	λ_{ave}^*	η^*
[-]	[cm/s]	[cm/s]	[1/cm ³]	[1/cm ³]	[V]	[cm ² /s]	[cm ² /s]	[cm ² /Vs]	[cm ² /Vs]	[nm]	[nm]	[%]	[nm]	[%]
5.00	40.00	3.84	8.43E+06	1.30E+08	0.80	0.25	0.25	9.65	9.65	160.00	35.56	20.46	7.11	21.20
10.00	20.00	1.92	8.43E+06	1.30E+08	0.82	0.50	0.50	19.30	19.30	160.00	35.56	21.85	3.56	22.67
20.00	10.00	0.96	8.43E+06	1.30E+08	0.86	1.00	1.00	38.61	38.61	160.00	35.56	23.46	1.78	24.34
30.00	6.67	0.64	8.43E+06	1.30E+08	0.90	1.50	1.50	57.91	57.91	160.00	35.56	24.43	1.19	25.35
40.00	5.00	0.48	8.43E+06	1.30E+08	0.94	2.00	2.00	77.22	77.22	160.00	35.56	25.06	0.89	26.00
60.00	3.33	0.32	8.43E+06	1.30E+08	1.01	3.00	3.00	115.82	115.82	160.00	35.56	25.84	0.59	26.82
80.00	2.50	0.24	8.43E+06	1.30E+08	1.09	4.00	4.00	154.43	154.43	160.00	35.56	26.37	0.48	27.36
100.00	2.00	0.19	8.43E+06	1.30E+08	1.17	5.00	5.00	193.04	193.04	160.00	35.56	26.77	0.40	27.77
120.00	1.67	0.16	8.43E+06	1.30E+08	1.25	6.00	6.00	231.65	231.65	160.00	35.56	27.10	0.34	28.11
140.00	1.43	0.14	8.43E+06	1.30E+08	1.32	7.00	7.00	270.26	270.26	160.00	35.56	27.37	0.29	28.40
160.00	1.25	0.12	8.43E+06	1.30E+08	1.40	8.00	8.00	308.87	308.87	160.00	35.56	27.61	0.25	28.65

Observations: (i) The values in boldface formatted numbers correspond to cell design 3 in Fig.4, and high-efficiency cell in Fig. 5; (ii) the values in italic formatted numbers correspond to the cell with $t_0 = 160$ nm in Fig. 3; * values obtained in f_B - constrained determination of λ_{ave} .

2

3 The curves in Fig. 3 visualize how the efficiency of a PSC in a certain development state can be
4 optimized by (i) the improvement of the material properties, as expressed by the f_B factor; (ii) light
5 trapping for a constant f_B factor, as used for $t_0 < 450$ nm; and (iii) the combination of these methods.
6 While material property improvements result in efficiency growths almost solely based on the
7 increase of V_{MPP} ; light trapping increases the efficiency as a function of both, a V_{MPP} rise, and
8 predominantly, an increase of J_{MPP} . Such improvements can be discussed comparing the optimization
9 results in Table 4 (Fig.4), which results in Table 5. Considering that the cell with the state-of-the-art
10 efficiency of 24.2 % is based on an effective light trapping scheme (Figure 3, design 9), a relative
11 efficiency rise of 14.6 % (Table 5 - line 13) can be obtained as a function of further material property
12 improvements. This increase is almost solely based on a 14.1 % rise of V_{MPP} and results in the
13 proposed cell design 3.

14

1
2
3
4
5
6
7
8
9
10
11
12
13
14
15
16
17
18
19
20
21
22
23
24
25
26
27
28

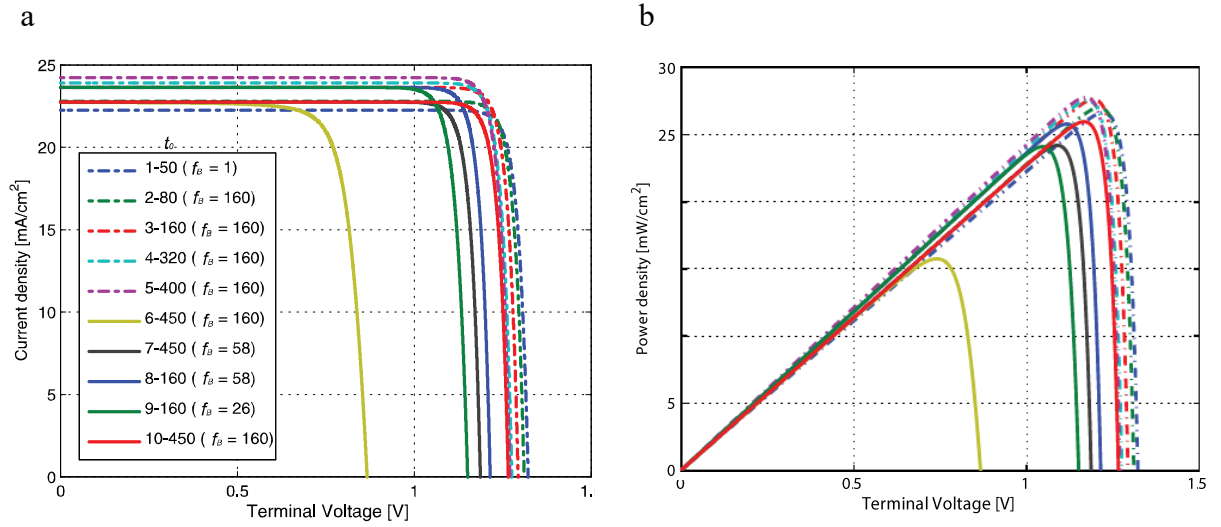


Fig. 4. (a) J-V and (b) power curves of different solar cell designs, as obtained by the multidimensional optimizations, as specified by the absorber layer thickness (t_0) and boundary amplification factor (f_B): (1) $t_0 = 50$ nm, $f_B = 160$; (2) $t_0 = 80$ nm, $f_B = 160$; (3) $t_0 = 160$ nm, $f_B = 160$; (4) $t_0 = 320$ nm, $f_B = 160$; (5) $t_0 = 400$ nm, $f_B = 160$; (6) $t_0 = 450$ nm, $f_B = 1$ (Sun et al., 2015); (7) $t_0 = 450$ nm, $f_B = 58 \approx$ state-of-the-art efficiency value; (8) $t_0 = 160$ nm, $f_B = 58$; (9) $t_0 = 160$ nm, $f_B = 26 \approx$ state-of-the-art efficiency value, (10) $t_0 = 450$ nm, $f_B = 160$.

Table 4
Optimization setup configurations and perovskite performance parameters extracted from the J-V curve characteristics for the cell designs as presented in Figs. 3 and 4.

Cell design	f_B [-]	t_0 [nm]	λ_{ave} [nm]	$q G_{max}(\#)$ [mA/cm ²]	J_{sc} [mA/cm ²]	V_{oc} [V]	J_{MPP} [mA/cm ²]	V_{MPP} [V]	FF [-]	PCE [%]
1	160	50	11.1	22.5	22.3	1.32	21.8	1.22	0.905	26.6
2	160	80	17.8	23.1	22.8	1.31	22.3	1.21	0.904	27.0
3	160	160	35.6	23.9	23.6	1.29	23.1	1.19	0.903	27.6
4	160	320	71.1	24.2	23.9	1.28	23.4	1.18	0.902	27.5
5	160	400	88.9	24.5	24.2	1.27	23.7	1.17	0.902	27.8
6	1	450	100.0	23.0	22.7	0.87	21.3	0.74	0.799	15.7
7	58	450	100.0	23.0	22.7	1.19	22.2	1.09	0.896	24.2
8	58	160	35.6	23.9	23.6	1.21	23.1	1.12	0.898	25.8
9	26	160	35.6	23.9	23.6	1.15	23.0	1.05	0.886	24.1
10	160	450	100.0	23.0	22.7	1.27	22.3	1.17	0.902	26.0

(#) Adopted short circuit current densities as obtained in (Cai et al. 2015). Observation: In the simplified Beer-Lambert model (Appendix B.1.1), the J_{sc} is to some minute extent lower than qG_{max} , as used in the setup of this model (see MatlabTM program in Supplementary Material), an effect which disappears for large values of $m > 10$ in equation (8). However, as in the present modeling an $m = 4.5$ is adopted, a feeble reduction of the J_{sc} , in comparison to qG_{max} , is obtained. A meliorated model of the short circuit current density would, therefore, result in slightly higher maximal efficiencies as here presented, because of the higher resulting J_{sc} values.

29
30
31
32
33
34

Table 5

Relative increase or decrease of different performance parameters in the comparison of several suggested design proposals.

Row	Design improvements	J_{sc} [%]	V_{oc} [%]	J_{MPP} [%]	V_{MPP} [%]	FF [%]	PCE [%]
1	Sun - Design 9	4.0	32.8	8.3	41.2	10.8	53.0
2	Sun - Design 7	0.1	36.9	4.5	47.0	12.1	53.6
3	Sun - Design 10	0.1	46.0	4.7	57.5	12.8	64.8
4	Sun - Design 3	4.0	49.2	8.8	61.2	13.0	75.3
5	Sun - Design 8	4.0	40.1	8.6	50.7	12.3	63.7
6	Design 7 - Design 8	3.9	2.3	4.0	2.5	0.2	6.6
7	Design 9 - Design 8	0.0	5.5	0.3	6.7	1.4	7.0
8	Design 9 - Design 7	-3.8	3.1	-3.5	4.1	1.2	0.4
9	Design 7 - Design 10	0.0	6.6	0.2	7.1	0.6	7.3
10	Design 8 - Design 10	-3.8	4.2	-3.7	4.5	0.4	0.7
11	Design 10 - Design 3	3.9	2.2	4.0	2.3	0.2	6.4
12	Design 8 - Design 3	0.0	6.5	0.1	6.9	0.6	7.1
13	Design 9 - Design 3	0.0	12.4	0.4	14.1	2.0	14.6
14	Design 7 - Design 3	3.9	9.0	4.1	9.6	0.8	14.1

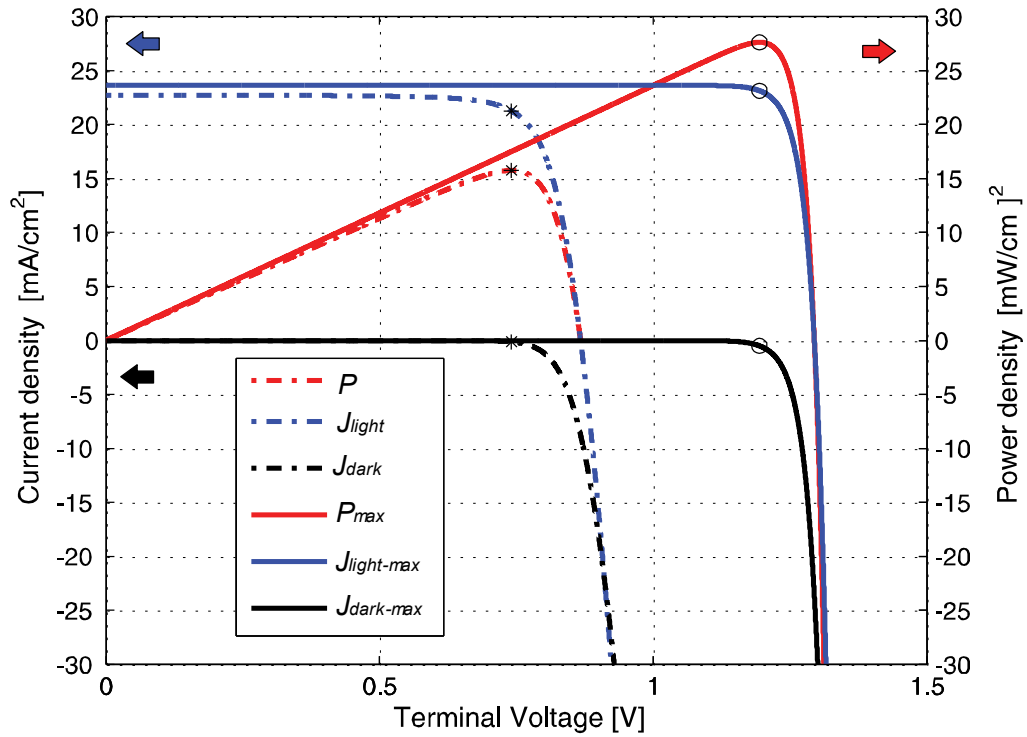


Fig. 5. J-V and power curves of the initial and optimized PSCs, with marked maximal power point (MPP) values: (i) curves for the solar cell configuration of the manufactured and modeled PSC in (Sun et al. 2015) (J_{light} , J_{dark} , P) and (ii) curves for the simulated solar cell model, as show for a multidimensional optimization, with an maximal PCE of 27.6 % for $f_B = 160$, $t_0 = 160$, ($J_{light-max}$, $J_{dark-max}$, P_{max}) for AM 1.5 reference solar irradiance of 100 mW/cm². Stars and circles show the MPP operation points of these curves with MPP power densities of 15.7 mW/cm² and 27.6 mW/cm², corresponding in this normalized presentation to efficiencies of $\eta_{MPP} = 15.7\%$ and 27.6% (Matlab™ program for the configuration of this figure as a function of the cell's material properties in Supplementary Material).

1 However, considering that the state-of-the-art cell is not based on light trapping (design 7); its PCE
2 can be increased by 6.6% using light trapping with spherical nanoparticles, as based on a 4% rise of
3 J_{MPP} and a 2.5% rise of V_{MPP} , obtaining design 8 (Table 5 - row 6). A similar relative increase is
4 obtained for cells with improved ($f_B \geq 58$, Fig. 3) and perfect material properties ($f_B = 160$, Table 5 -
5 row 11). Further material property improvements in design 8 can raise the PCE by 7%, as based on a
6 6.9% rise of the V_{MPP} , obtaining cell design 3 (Table 5 - row 12). If no light trapping is considered at
7 all, the state-of-the-art efficiency (design 7) can be increased by 7.3%, as almost only based on a
8 7.1% V_{MPP} rise, obtaining cell design 10 (Table 5 - row 9), which presents the here considered most
9 ideal material properties with $f_B = 160$. The efficiency of 26%, as obtained by design 10 ($f_B = 160$),
10 can also be obtained with a much lower property improvement factor of $f_B \approx 62$, if light trapping is
11 used in a PSC with a $t_0 = 160$ nm (horizontal dotted line in Fig. 3). Finally, the highest efficiency
12 increase (14.1 %) of design 7 is obtained, using light trapping and material property improvements
13 combined, resulting in design 3, as based on a 9.6% increase of the V_{MPP} and a 4.1% increase of the
14 J_{MPP} (Table 5 - row 14).

15 Fig. 5 compares the two J-V curves, and its power curves, of (i) the cell as optimized in (Sun et al.,
16 2015) (dash-dotted curves), and (ii) the here considered, most ideal cell design. The latter was
17 obtained by a multidimensional optimization of a cell with spherical plasmonic nanoparticles in a
18 160 nm thick absorber layer (Table 3 - cell design 3). The PCE of this cell is only 0.2 % lower in
19 comparison to the highest obtained efficiency in a cell with $t_0 = 400$ nm (Fig. 3, Table 2). The
20 improvement of the cell's material properties and the light trapping with spherical nanoparticles
21 result in a significant PCE increase from 15.7% to 27.6%.

22

23 **5 Discussions**

24 Summing up the nine one-dimensional efficiency increases, as presented in Table A.1, we register a
25 total contribution of 4.5%, for a boundary amplification factor of $f_B = 160$. However, the combined
26 contribution of these variables, in a multidimensional optimization, results with the maximum value

1 of 27.6% (Table 3) in a much higher efficiency rise of $27.6\% - 15.7\% = 13.4\%$, considering the same
2 f_B factor. Consequently, because of the summed single contributions of the one-dimensional PCE
3 increases, the efficiency raises by 4.5%, and because of further effects, a much higher growth, with
4 the value of $13.4\% - 4.5\% = 8.9\%$ can be obtained. We registered a similar behavior also in the
5 comparison of one- and two-dimensional optimizations (Appendix, Section A.1) and assign this large
6 additional PCE increase to the nonlinearities, as inherent to the analyzed PSC and its drift-diffusion
7 model. As a result, higher-dimensional optimizations are much more effective, in comparison to the
8 state-of-the-art one- and two-dimensional optimizations.

9 The proper efficiency growth in Fig. 3 presents also a nonlinear behavior, as the highest PCE
10 gradients are obtained for low f_B values, which correspond to small material property improvements
11 in the hypercube space. Hence, the multidimensional efficiency optimization is most effective for
12 cells, which efficiency is close, or lower than the state-of-the-art PCE with $f_B \approx 58$, as minor
13 modifications in the material properties, lead to the highest efficiency gradients. Light trapping
14 enhances this effectiveness in the multidimensional optimizations, because of the higher gradients of
15 the related curves in Fig. 3.

16 The highest and second-highest values of J_{sc} and J_{MPP} are obtained by the light trapping cell designs
17 5 and 4, presenting the absorber layer thicknesses of $t_0 = 400$ and 320 nm (Table 4). Meanwhile, the
18 largest and second-largest values of the efficiencies are obtained by cell designs 5 and 3, presenting a
19 t_0 of 400 and 160 nm. In the case of V_{OC} and V_{MPP} , the highest values are surprisingly obtained for the
20 cell with the thinnest absorber layer (design 1), resulting inclusively to the largest FF, which means
21 that V_{OC} and V_{MPP} decrease proportionally with the increase of t_0 (Table 3). As a result of these
22 effects, thin absorber layers result in reasonable high efficiencies, obtaining thus the second-highest
23 PCE with the selected favorite cell, which presents an absorber layer of $t_0 = 160$ nm (design 3).
24 We account the increases in V_{OC} and FF, on the concomitant (i) reduction of t_0 , and (ii) the light
25 trapping effect, which result in its combination to high PCEs. The high V_{OC} is a function of the
26 photon recycling effect, as inherent to PSCs (Pazos-Outón et al., 2016), which increases by light

1 trapping (Sha et al., 2015 and Kirchartz et al., 2016), and results furthermore in a larger fill factor
2 (FF) (Sha et al., 2015). Thin absorber layers present lower recombination of charge carriers, as
3 discussed in (Domanski et al., 2016) and Appendix A.5. As a result, thin absorber layers increase the
4 FF and the V_{oc} , even without light trapping, as shown by numerical simulations in (Devi et al., 2018).
5 The lower absorber layer thicknesses can be manufactured with ultra-thin coating techniques (Liu,
6 2017), and the solvent-solvent extraction methods (Zhou et al., 2015), where the latter results in
7 smooth, and thickness adjustable absorber layers, in a large range of $t_0 = 20 \dots 410$ nm.
8 PSCs with $t_0 \approx 450$ nm do already present a low Pb content, which is similar, to the heavy-metal
9 content of state-of-the-art silicon photovoltaic modules (Green et al., 2014; Stasiulionis, 2015).
10 Fortunately, the here presented thickness reduction of the absorber layer to $t_0 = 160$ nm leads to an
11 additional reduction of the Pb residual.

12 The here used modeling of the short circuit current density presents high accuracies for the cases: (i)
13 without light trapping, and (ii) light trapping with spherical nanoparticles; because the setup of the
14 short circuit current density is based on high-resolution simulations, such as (i) the OTM modeling
15 (Sun et al., 2015), and (ii) the FDTD modeling (Cai et al., 2015) (Appendix section B.1.4).
16 Furthermore, we consider reasonable low uncertainties in the Beer-Lambert modeling (Appendix
17 B.1.1 to B.1.3). Additionally, we remark that large deviations in λ_{ave} value result in very small
18 efficiency deviations for the same f_B (Tables 1 to 3). Therefore, even under a hypothetical
19 consideration of large uncertainties in the Beer-Lambert law, and its related λ_{ave} , only small
20 uncertainties of the optimized efficiency values would be obtained.

21 The highest here achieved efficiency for single-junction PSCs of 27.76% (Table 2), is higher than (i)
22 the state-of-the-art efficiency of 24.2 % and (ii) the highest simulated efficiency of 25% (Agarwal
23 and Nair, 2014, 2015). In fact, a large set of our optimized design proposals, as presented in Fig. 3,
24 increase the state-of-the-art PCEs of manufactured and simulated solar cells. As expected, all
25 proposals present a lower efficiency than (i) the lowest value of the theoretical upper limit with PCE

1 = 29.9%, as considered for zero surface recombination velocities and ideal light trapping (Ren et al.,
2 2017).

3 The material property improvements as selected by the multidimensional optimization algorithm are
4 general and must not coincide with property values of manufactured PSCs, as improvements of the
5 different properties can appear at individual scales in those cells. We used the general property
6 improvement, as expressed by f_B in order to: (i) illustrate the large efficiency advantage of
7 multidimensional property improvements; (ii) present high- and highest-performance cell designs
8 with low Pb content, and discuss by which techniques these cells can be manufactured; (iii) estimate
9 and discuss the percentual improvements of several performance parameters, comparing cells in
10 different development states, or cell designs; (iv) identify dependencies in-between model variables,
11 as appeared between t_0 and λ_{ave} (Table A.2 and Figs. 2a and 2b); (v) present a complete set of
12 possible two-dimensional sensitivity analyses (Appendix A.1); and (vi) identified from the latter
13 analyses that s_f , s_b , t_0 , λ_{ave} and D_p are the most important optimization variables, in this order. As a
14 result, we get a better understanding and provide useful knowledge for the efficiency optimization of
15 manufactured PSCs. The presented results can be used as a roadmap, showing to which extend a
16 PSC's performance parameters and its efficiency can be increased, by different measures and in
17 several development states, while its Pb content is reduced. In our design proposals, we consider one,
18 two (Table A.1), and multidimensional improvements of the cell's material properties (Fig. 3); which
19 are combined with light trapping, and thin-film coating techniques.

20 Whereas material property improvements lead to the highest relative efficiency increase in cells,
21 which PCE is less or equal to the state-of-the-art efficiency (Fig. 3, Table 5 - row 2), light trapping
22 techniques are most efficient to improve the efficiency in cells, which PCE is higher or equal than
23 the state-of-the-art PCE (Fig. 3, Table 5 - rows 6 and 11). While the former is almost solely based on
24 V_{MPP} increase, the latter increase both, the J_{MPP} and the V_{MPP} . Being the state-of-the-art efficiency
25 based on light trapping (cell design 9) or not (cell design 7), the cell's efficiency can be increased by:

1 (i) further material property improvements (Table 5 - row 13), and (ii) its combination with light
2 trapping (Table 5 - row 14), resulting in both cases to a PCE increase of approximately 14%.
3 The λ_{ave} should be always determined as a function of t_0 , being this in an m -constraint or a f_B -
4 constrained relationship, where the former is simply to calculate, and the results in slightly higher
5 efficiency values (Table 1 to 3 - last two columns), if very low reflection losses are configurable. As
6 the remaining properties stand not in a relationship, the here presented multidimensional
7 optimizations can be substituted by simple model simulations, in cell manufacturing and research,
8 adopting the two-dimensional sensitivity analysis, as presented in Fig. 2f; and alternatively, using the
9 constraint condition in equation (9). We suggest that PSC manufacturing should be based on
10 thickness adjustable thin-film coating techniques (Zhou et al., 2015, Liu, 2017), where an ideal t_0 can
11 be adjusted as a function of a configured λ_{ave} . Otherwise, adjustable light trapping techniques (Cai et
12 al., 2015) may be used to configure an adjustable ideal λ_{ave} , for a fixed absorber layer thickness. We
13 also like to advise that some solar cell types have an ideal built-in field (Green, 2009), as related to
14 an ideal built-in voltage, an effect that was not observed with the present model in the constraint of
15 $V_{bi} \leq 1.4$ V.

17 **6. Conclusions**

18 Our analyses lead to a better understanding of the cell's optimization process, and we propose high-
19 efficiency PSC designs with ultra-thin absorber layers with a significant lower Pb content. The high
20 PCE values for the absorber layer thickness of 160 nm, are obtained as light trapping shows similar
21 current densities for a wide range of absorber layer thicknesses, and as V_{OC} and V_{MPP} increase as a
22 function of the thickness reduction of the absorber layer. We demonstrate and discuss a large
23 efficiency advantage, in multidimensional optimizations, and assign this effect to the nonlinear
24 behavior of the drift-diffusion model of electrons and holes. As discussed, our optimizations result in
25 PCE values, which appear in expected, and reasonable, ranges of the efficiency, and we consider low
26 uncertainties for simulated design proposals. We obtained high sensitivities for low f_B values, and

1 these sensitivities improve with light trapping. Furthermore, light trapping is most efficient for high
2 f_B values, which result in the highest PCE increases. Therefore, light trapping is always
3 advantageous. For high f_B factors, as it leads to the highest PCE rises, and for low f_B factors, as it not
4 only increases the efficiency but also helps to improve the sensitivity of the further model variables.
5 However, researchers which like to optimize PSCs with efficiencies much lower than the state-of-
6 the-art PCE should focus principally on the improvement of the material properties, by reason of the
7 resulting high PCE gradients in this range.

8

9 **Future works**

10 Further FDTD simulations for cells with shape optimized nanoparticles (Appendix sections A.2 and
11 B.1.5) and special cell designs with high J_{sc} values (Appendix section A.6 and Table A.4) should be
12 accomplished. A protocol for the multidimensional material property measurement and control
13 should be developed in the research with the manufactured prototypes.

1 Nomenclature

2

D_n	Diffusion coefficient of electrons [cm^2/s],
D_p	Diffusion coefficient of holes [cm^2/s],
f_B	Boundary expansion factor [-],
$G_{AM1.5}$	Solar irradiance with air mass 1.5 [mW/cm^2]
$G(x)$	Generation rate of charges as a function of x [$\text{s}^{-1}\text{cm}^{-3}$],
G_{eff}	Effective charge carrier generation [$\text{s}^{-1}\text{cm}^{-3}$],
G_{max}	Maximal or total charge carrier generation [$\text{s}^{-1}\text{m}^{-2}$]
J_b	Electron recombination current density of the back charge conduction layer at $x = t_0$ [mA/cm^2],
J_{dark}	Measurable current density in the dark [mA/cm^2],
J_f	Electron recombination current density of the front charge conduction layer at $x = 0$ [mA/cm^2],
J_{light}	The measurable current density under light exposure [mA/cm^2],
$J_{MPP,i}$	Maximal power point current density [mA/cm^2],
J_n	Electron current density at the back charge conduction layer [mA/cm^2],
J_p	Hole current density at the front charge conduction layer [mA/cm^2],
J_{sc}	Short circuit current density [mA/cm^2],
m	Factor which relates t_0 and λ_{ave} in the Beer-Lambert law [-],
P_{MPP}	Maximal power point power density [mW/cm^2],
k_B	Boltzmann constant $1.38064852 \times 10^{-23}$ [J/K],
q	Electric charge of an electron or hole [mAs],
s_f	Surface recombination velocity of electrons (s_n) [cm/s],
s_b	Surface recombination velocity of holes (s_p) [cm/s],
T	Cell temperature [K],
t_0	Absorber layer thickness [nm],
t_{0-min}	Minimal absorber layer thickness [nm],
t_{0-min}	Minimal necessary absorber layer thickness [nm],
V	Terminal voltage of the solar cell [V],
V_{bi}	Built-in voltage [V],
V_{MPP}	Maximal power point voltage [V],

V_{oc}	Open-circuit voltage [V],
$x = 0 \dots t_0$	Solar irradiance penetration depth [m],
$X_j = X_1 \dots X_9$	X_j is one of the nine model variables of the PSC model,
$X_{j,me}$	A model variable extracted from the measured J-V curve, X_j , is one of the nine model variables of the PSC model,
$X_{j,min} \dots X_{j,max}$	Variable expansion range for the variable j,

Greek symbols

Δn	Excess minority carrier concentration of electrons [cm^{-3}],
Δp	Excess minority carrier concentration of holes [cm^{-3}],
η_i	Optimized PCE for the i-th optimization iteration [%],
η_{max}	Optimized efficiency value [%],
λ	Wavelength of the solar irradiance [nm],
λ_{ave}	Average optical decay length [nm].
μ_n	Drift coefficient or mobility of electrons [$\text{cm}^2\text{V}^{-1}\text{s}^{-1}$]
μ_p	Drift coefficient or mobility of holes [$\text{cm}^2\text{V}^{-1}\text{s}^{-1}$]

1

Indices

$i = 1 \dots N$	Iterations in the optimization of the efficiency,
$k = 1 \dots M$	Iterations in the optimization of the power curve,
$j = 1 \dots 9$	Index, which counts the nine variables,

2

3

4

Declaration of Competing Interests

5

6

This manuscript does not have any conflict of interest.

7

8

9

Acknowledgments

10

11

12

13

The authors thank (i) Comissão de Aperfeiçoamento de Pessoal do Nível Superior (CAPES), (ii) Fotovoltaica UFSC - Grupo de Pesquisa Estratégica em Energia Solar at Universidade Federal de Santa Catarina and (iii) Agência Nacional de Energia Elétrica (ANNEEL) for their financial support.

14

15

Appendix

16

17

The appendix and supporting material associated with this article can be found, on the online version:

18

18

1 **References**

- 2 Adinolfi, V., Peng, W., Walters, G., Bakr, O.M., Sargent, E.H., 2017. The electrical and optical
3 properties of organometal halide perovskites relevant to optoelectronic performance. *Advanced*
4 *Materials*, 1-13.
- 5 Agarwal, S., Nair, P.R., 2014. Performance optimization for Perovskite based solar cells,
6 Proceedings of the 40th IEEE Photovoltaic Specialist Conference (PVSC). Colorado, pp. 1515-
7 1518.
- 8 Agarwal, S., Nair, P.R., 2015. Device engineering of perovskite solar cells to achieve near ideal
9 efficiency. *Applied Physics Letters* 107(12), 1-5.
- 10 Algora, C., Díaz, V., 2000. Influence of series resistance on guidelines for manufacture of
11 concentrator p-on-n GaAs solar cells. *Progress in Photovoltaics: Research and Applications*
12 8(2), 211-225.
- 13 Amu, T.L., 2014. Performance optimization of tin halide perovskite solar cells via numerical
14 simulation, (Master thesis). African University of Science and Technology, Abuja, Nigeria.
- 15 Atwater, H.A., Polman, A., 2010. Plasmonics for improved photovoltaic devices. *Nature materials*
16 9(3), 205-213.
- 17 Azri, F., Meftah, A., Sengouga, N., Meftah, A., 2019. Electron and hole transport layers optimization
18 by numerical simulation of a perovskite solar cell. *Solar Energy* 181, 372-378.
- 19 Ball, J.M., Stranks, S.D., Hörantner, M.T., Hüttner, S., Zhang, W., Crossland, E.J., Ramirez, I.,
20 Riede, M., Johnston, M.B., Friend, R.H., 2015. Optical properties and limiting photocurrent of
21 thin-film perovskite solar cells. *Energy & Environmental Science* 8(2), 602-609.
- 22 Bazzo, T.d.P.M., Kölzer, J.F., Carlson, R., Wurtz, F., Gerbaud, L., 2017. Multiphysics design
23 optimization of a permanent magnet synchronous generator. *IEEE Transactions on Industrial*
24 *Electronics* 64(12), 9815-9823.
- 25 Brittman, S., Adhyaksa, G.W.P., Garnett, E.C., 2015. The expanding world of hybrid perovskites:
26 Materials properties and emerging applications. *MRS Communications* 5(01), 7-26.
- 27 Burschka, J., Pellet, N., Moon, S.-J., Humphry-Baker, R., Gao, P., Nazeeruddin, M.K., Grätzel, M.,
28 2013. Sequential deposition as a route to high-performance perovskite-sensitized solar cells.
29 *Nature* 499(7458), 316-319.
- 30 Byrd, R.H., Hribar, M.E., Nocedal, J., 1999. An interior point algorithm for large-scale nonlinear
31 programming. *SIAM Journal on Optimization* 9(4), 877-900.
- 32 Cai, B., Peng, Y., Cheng, Y.-B., Gu, M., 2015. 4-fold photocurrent enhancement in ultrathin
33 nanoplasmonic perovskite solar cells. *Optics Express* 23(24), A1700-A1706.
- 34 Chowdhury, M., Alam, M., 2014. A physics-based analytical model for bulk heterojunction organic
35 solar cells incorporating monomolecular recombination mechanism. *Current Applied Physics*
36 14(3), 340-344.
- 37 Crow, M.L., 2009. *Computational methods for electric power systems*. Crc Press.
- 38 Devi, C., Mehra, R., 2019. Device simulation of lead-free MASnI₃ solar cell with CuSbS₂ (copper
39 antimony sulfide). *Journal of Materials Science* 54(7), 5615-5624.
- 40 Devi, N., Parrey, K.A., Aziz, A., Datta, S., 2018. Numerical simulations of perovskite thin-film solar
41 cells using a CdS hole blocking layer. *Journal of Vacuum Science & Technology B,*
42 *Nanotechnology and Microelectronics: Materials, Processing, Measurement, and Phenomena*
43 36(4), 04G105.
- 44 Dixit, H., Punetha, D., Pandey, S.K., 2019. Improvement in performance of lead free inverted
45 perovskite solar cell by optimization of solar parameters. *Optik* 179, 969-976.
- 46 Domanski, K., Correa-Baena, J.-P., Mine, N., Nazeeruddin, M.K., Abate, A., Saliba, M., Tress, W.,
47 Hagfeldt, A., Grätzel, M., 2016. Not all that glitters is gold: Metal-migration-induced
48 degradation in perovskite solar cells. *ACS Nano* 10(6), 6306-6314.
- 49 Foster, J.M., Snaith, H.J., Leijtens, T., Richardson, G., 2014. A model for the operation of perovskite
50 based hybrid solar cells: Formulation, analysis, and comparison to experiment. *SIAM Journal*
51 *on Applied Mathematics* 74(6), 1935-1966.

1 Green, M., A., 2009. Do built-in fields improve solar cell performance? *Progress in Photovoltaics: Research and Applications* 17(1), 57-66.

2

3 Green, M.A., Ho-Baillie, A., Snaith, H.J., 2014. The emergence of perovskite solar cells. *Nature Photonics* 8(7), 506-514.

4

5 Huang, H., Huang, J., 2014. *Organic and hybrid solar cells*, first ed. Springer, New York.

6 Iftiqar, S.M., Yi, J., 2016. Numerical simulation and light trapping in perovskite solar cell. *Journal of Photonics for Energy* 6(2), 1-10.

7

8 Jiang, Y., Green, M.A., Sheng, R., Ho-Baillie, A., 2015. Room temperature optical properties of organic-inorganic lead halide perovskites. *Solar Energy Materials and Solar Cells* 137, 253-257.

9

10

11 Jung, E.H., Jeon, N.J., Park, E.Y., Moon, C.S., Shin, T.J., Yang, T.-Y., Noh, J.H., Seo, J., 2019. Efficient, stable and scalable perovskite solar cells using poly (3-hexylthiophene). *Nature* 567(7749), 511.

12

13

14 Kakavelakis, G., Petridis, K., Kymakis, E., 2017. Recent advances in plasmonic metal and rare-earth-element upconversion nanoparticle doped perovskite solar cells. *Journal of Materials Chemistry A* 5(41), 21604-21624.

15

16

17 Kanoun, A.-A., Kanoun, M.B., Merad, A.E., Goumri-Said, S., 2019. Toward development of high-performance perovskite solar cells based on CH₃NH₃GeI₃ using computational approach. *Solar Energy* 182, 237-244.

18

19

20 Kim, H.D., Ohkita, H., 2017. Potential Improvement in Fill Factor of Lead-Halide Perovskite Solar Cells. *Solar RRL* 1(6), 1-6.

21

22 Kirchartz, T., Staub, F., Rau, U., 2016. Impact of photon recycling on the open-circuit voltage of metal halide perovskite solar cells. *ACS Energy Letters* 1(4), 731-739.

23

24 Kojima, A., Teshima, K., Shirai, Y., Miyasaka, T., 2009. Organometal halide perovskites as visible-light sensitizers for photovoltaic cells. *Journal of the American Chemical Society* 131(17), 6050-6051.

25

26

27 Kratzenberg, M., Rambo, C., R  ther, R., Beyer, H., 2015. Sensitivity analyses of a p-i-n perovskite solar cell with a fixed band gap, in: Society, I.S.E. (Ed.) *Solar World Congress*. Daegu, Korea, pp. 1-5.

28

29

30 Liu, C., Li, W., Fan, J., Mai, Y., 2018. A brief review on the lead element substitution in perovskite solar cells. *Journal of Energy Chemistry* 27(4), 1054-1066.

31

32 Liu, F., Zhu, J., Wei, J., Li, Y., Lv, M., Yang, S., Zhang, B., Yao, J., Dai, S., 2014. Numerical simulation: toward the design of high-efficiency planar perovskite solar cells. *Applied Physics Letters* 104(25), 1-4.

33

34

35 Liu, Y., 2017. *Plasmonic metal nanoparticle films for solar cells with ultra-thin absorber layers: Low temperature synthesis and application*. (Doctoral thesis), Freie Universit  t, Berlin, Germany.

36

37 Martynov, Y.B., Nazmitdinov, R.G., Moia-Pol, A., Gladyshev, P.P., Tameev, A.R., Vannikov, A.V., Pudlak, M., 2017. On the efficiency limit of ZnO/CH₃NH₃PbI₃/CuI perovskite solar cells. *Physical Chemistry Chemical Physics* 19(30), 19916-19921.

38

39

40 NREL, 2019. Best Research-Cell Efficiencies, National Renewable Energy Laboratory - Photovoltaic Research Homepage.

41

42 O'Regan, B., Gr  tzel, M., 1991. A low-cost, high-efficiency solar cell based on dye-sensitized colloidal TiO₂ films. *Nature* 353(6346), 737-740.

43

44 Park, J.-K., Kang, J.-C., Kim, S.Y., Son, B.H., Park, J.-Y., Lee, S., Ahn, Y.H., 2012. Diffusion length in nanoporous photoelectrodes of dye-sensitized solar cells under operating conditions measured by photocurrent microscopy. *The Journal of Physical Chemistry Letters* 3(23), 3632-3638.

45

46

47

48 Pazos-Out  n, L.M., Szumilo, M., Lamboll, R., Richter, J.M., Crespo-Quesada, M., Abdi-Jalebi, M., Beeson, H.J., Vru  ini  , M., Alsari, M., Snaith, H.J., 2016. Photon recycling in lead iodide perovskite solar cells. *Science* 351(6280), 1430-1433.

49

50

1 Qiu, W., Merckx, T., Jaysankar, M., de la Huerta, C.M., Rakocevic, L., Zhang, W., Paetzold, U.,
2 Gehlhaar, R., Froyen, L., Poortmans, J., 2016. Pinhole-free perovskite films for efficient solar
3 modules. *Energy & Environmental Science* 9(2), 484-489.

4 Ren, X., Wang, Z., Sha, W.E., Choy, W.C., 2017. Exploring the way to approach the efficiency limit
5 of perovskite solar cells by drift-diffusion model. *Acs Photonics* 4(4), 934-942.

6 Rong, Y., Hou, X., Hu, Y., Mei, A., Liu, L., Wang, P., Han, H., 2017. Synergy of ammonium
7 chloride and moisture on perovskite crystallization for efficient printable mesoscopic solar cells.
8 *Nature Communications* 8, 1-8.

9 Rühle, S., 2016. Tabulated values of the Shockley-Queisser limit for single junction solar cells. *Solar*
10 *Energy* 130, 139-147.

11 Rüther, R., Kleiss, G., Reiche, K., 2002. Spectral effects on amorphous silicon solar module fill
12 factors. *Solar Energy Materials and Solar Cells* 71(3), 375-385.

13 Sha, W.E., Ren, X., Chen, L., Choy, W.C., 2015. The efficiency limit of $\text{CH}_3\text{NH}_3\text{PbI}_3$ perovskite
14 solar cells. *Applied Physics Letters* 106(22), 1-5.

15 Shockley, W., Queisser, H.J., 1961. Detailed balance limit of efficiency of p-n junction solar cells.
16 *Journal of Applied Physics* 32(3), 510-519.

17 Stasiulionis, J., 2015. Life cycle assessment of perovskite solar cells and comparison to silicon solar
18 cells, (Master thesis). Chalmers University of Technology, Sweden, p. 50.

19 Sun, X., Asadpour, R., Nie, W., Mohite, A.D., Alam, M.A., 2015. A physics-based analytical model
20 for perovskite solar cells. *IEEE Journal of Photovoltaics* 5(5), 1389-1394.

21 Taretto, K., Soldera, M., Koffman-Frischknecht, A., 2017. Material Parameters and Perspectives for
22 Efficiency Improvements in Perovskite Solar Cells Obtained by Analytical Modeling. *IEEE*
23 *Journal of Photovoltaics* 7(1), 206-213.

24 Wong, W.-Y., Wang, X.-Z., He, Z., Djurišić, A.B., Yip, C.-T., Cheung, K.-Y., Wang, H., Mak,
25 C.S.K., Chan, W.-K., 2007. Metallated conjugated polymers as a new avenue towards high-
26 efficiency polymer solar cells. *Nature Materials* 6(7), 521-527.

27 Yin, W.-J., Shi, T., Yan, Y., 2014. Unique properties of halide perovskites as possible origins of the
28 superior solar cell performance. *Advanced Materials* 26(27), 4653-4658.

29 Zandi, S., Razaghi, M., 2019. Finite element simulation of perovskite solar cell: A study on
30 efficiency improvement based on structural and material modification. *Solar Energy* 179, 298-
31 306.

32 Zhao, P., Liu, Z., Lin, Z., Chen, D., Su, J., Zhang, C., Zhang, J., Chang, J., Hao, Y., 2018. Device
33 simulation of inverted $\text{CH}_3\text{NH}_3\text{PbI}_{3-x}\text{Cl}_x$ perovskite solar cells based on PCBM electron
34 transport layer and NiO hole transport layer. *Solar Energy* 169, 11-18.

35 Zhou, Y., Yang, M., Wu, W., Vasiliev, A.L., Zhu, K., Padture, N.P., 2015. Room-temperature
36 crystallization of hybrid-perovskite thin films via solvent-solvent extraction for high-
37 performance solar cells. *Journal of Materials Chemistry A* 3(15), 8178-8184.

38